Published in final edited form as:
*J Biomech*. 2014 November 28; 47(15): 3605–3612. doi:10.1016/j.jbiomech.2014.10.011.

# The Effects of Tensile-Compressive Loading Mode and Microarchitecture on Microdamage in Human Vertebral Cancellous Bone

**Floor M. Lambers**[a], **Amanda R. Bouman**[a], **Evgeniy V. Tkachenko**[a], **Tony M. Keaveny**[d], and **Christopher J. Hernandez**[a,b,c]

[a]Sibley School of Mechanical and Aerospace Engineering, Cornell University, Ithaca, NY, USA

[b]Department of Biomedical Engineering, Cornell University, Ithaca, NY, USA

[c]Hospital for Special Surgery, New York, NY, USA

[d]Departments of Mechanical Engineering and Bioengineering, University of California, Berkeley, CA, USA

## Abstract

The amount of microdamage in bone tissue impairs mechanical performance and may act as a stimulus for bone remodeling. Here we determine how loading mode (tension v. compression) and microstructure (trabecular microarchitecture, local trabecular thickness, and presence of resorption cavities) influence the number and volume of microdamage sites generated in cancellous bone following a single overload. Twenty paired cylindrical specimens of human vertebral cancellous bone from 10 donors (47–78 years) were mechanically loaded to apparent yield in either compression or tension, and imaged in three dimensions for microarchitecture and microdamage (voxel size 0.7 × 0.7 × 5.0 μm). We found that the overall proportion of damaged tissue was greater ($p=0.01$) for apparent tension loading (3.9 ± 2.4%, mean ± SD) than for apparent compression loading (1.9 ± 1.3%). Individual microdamage sites generated in tension were larger in volume ($p < 0.001$) but not more numerous ($p = 0.64$) than sites in compression. For both loading modes, the proportion of damaged tissue varied more across donors than with bone volume fraction, traditional measures of microarchitecture (trabecular thickness, trabecular separation, etc.), apparent Young's modulus, or strength. Microdamage tended to occur in regions of greater trabecular thickness but not near observable resorption cavities. Taken together, these



**Corresponding Author:** Prof. Christopher J Hernandez, Cornell University, Sibley School of Mechanical and Aerospace Engineering, 219 Upson Hall, Ithaca, NY 14853, USA Phone: (607) 255 5129, Fax: (607) 255 1222, cjh275@cornell.edu. fml42@cornell.edu, arb263@cornell.edu, evgeniy.v.tkachenko@gmail.com, tmk@me.berkeley.edu, cjh275@cornell.edu



**Author contributions** Conceived and designed the experiments: FML CJH TMK. Image acquisition: EVT. Image processing and data analysis: FML ARB EVT. Wrote the article: FML CJH. Critical revision and final approval of the manuscript: FML ARB EVT TMK CJH.

**Conflict of interest statement** Dr. Keaveny has served as a consultant for Amgen, Merck, and Agnovos and consults for and has a financial interest in O.N. Diagnostics. All other authors have no disclosures related to this work.

findings indicate that, regardless of loading mode, accumulation of microdamage in cancellous bone after monotonic loading to yield is influenced by donor characteristics other than traditional measures of microarchitecture, suggesting a possible role for tissue material properties.

**Keywords**

Bone Mechanics; Microdamage; Cancellous Bone; Microarchitecture; Resorption Cavities

## Introduction

Microscopic tissue damage in cancellous bone, referred to here as microdamage, impairs stiffness, strength and fatigue life (Hernandez and Keaveny, 2006; Hernandez et al., 2014; Lambers et al., 2013; Wachtel and Keaveny, 1997a) and is also thought to stimulate bone resorption and remodeling (Herman et al., 2010; Mori and Burr, 1993). The amount and morphology of microdamage formed in bone is likely influenced by apparent loading mode, microarchitecture and tissue material properties.

In cancellous bone, the microstructure allows for load redistribution as localized regions are damaged, such that increases in microdamage may be due to the initiation of new locations of microdamage or to the extension of already existing microdamage. Extension of existing microdamage sites is more likely to lead to trabecular microfracture, which has a disproportionate negative effect on mechanical performance of cancellous bone (Silva and Gibson, 1997; Yeh and Keaveny, 2001). The degree to which a microdamage site extends can be influenced by loading mode (Wang et al., 2005; Wu et al., 2013). Microdamage generated in cancellous bone is commonly identified with a bulk stain and evaluated in two-dimensional sections (Burr et al., 1997; Moore and Gibson, 2003; Moore and Gibson, 2002; Vashishth et al., 2000). Two-dimensional assessment of microdamage is useful for characterizing whole specimen amounts of damage, but cannot provide accurate measures of the number or size of damage sites. Three-dimensional assessment of microdamage in cancellous bone has recently been demonstrated (Bigley et al., 2008; Slyfield et al., 2012; Tang and Vashishth, 2007, 2010) and could measure the number, size and shape of individual microdamage sites, but has so far only been applied to study microdamage generated by apparent compression.

Theoretical and experimental models suggest that more tissue will yield under apparent tension than under apparent compression as a result of difference in local tissue failure modes (failure due to excessive tensile principal strains v. compressive principal strains) (Bayraktar and Keaveny, 2004), suggesting that apparent tension will result in more microdamage than apparent compression. In addition to apparent loading mode, trabecular microarchitecture, and local geometry such as the presence of resorption cavities or thickness of individual trabeculae, have also been implicated as factors that may influence the generation of microdamage (Green et al., 2011; Slyfield et al., 2012). To our knowledge, differences in microdamage generation between tensile and compressive loading have not been assessed using three-dimensional analysis and it is not known how the number and size of microdamage sites varies among the apparent loading modes. Additionally, the effect of

whole specimen microarchitecture and local geometry (including the presence of resorption cavities and thickness of trabeculae) on the generation of microdamage in these two apparent loading modes is not known.

The long-term goal of this research is to understand the generation of microdamage in cancellous bone and its effect on apparent mechanical properties. Specifically, in this study we consider a single uniaxial load and determine 1) the differences in the number and volume of microdamage sites in cancellous bone subjected to apparent tension or compression; 2) the effect of the cancellous microarchitecture and local microstructure on the number and size of microdamage sites; and 3) the degree to which microdamage formed under the two loading modes is spatially related to resorption cavities.

## Material and Methods

### Overview

Two specimens of vertebral cancellous bone were collected from each donor then loaded in either compression or tension. The resulting amount of microdamage was determined using three-dimensional imaging and the number and size of individual microdamage sites was determined along with traditional measures of microarchitecture and local trabecular thickness. The spatial association between microdamage and resorption cavities was also evaluated.

### Specimen preparation and mechanical testing (additional details in Supplementary Materials)

The fourth lumbar vertebral bodies of 10 donors (8 male, aged 47–78 years, 70 ± 10, mean ± SD, 2 female, aged 72, 80, tissue source National Disease Research Interchange, Philadelphia, PA, USA) with no medical history of metabolic bone disease or cancer and no obvious vertebral deformities were included in the study. Cylindrical cores of cancellous bone (nominal diameter 8 mm, nominal height 25–30 mm, nominal effective gage length 15 mm) aligned in the superior-inferior direction were collected using a diamond tipped coring tool. Two specimens were collected from each vertebra resulting in a total of 20 specimens. Due to errors in image acquisition, two specimens were excluded, resulting in 18 specimens (8 pairs and 2 single samples).

Specimens were stained with xylenol orange (0.5 mM in PBS, 2 hours) to label preexisting microdamage. Specimens were then potted into brass fixtures using bone cement in preparation for mechanical loading (Bevill et al., 2009). Microscopic tissue damage was induced by applying a single load to 0.8% strain (~apparent yield) in compression (n = 9) or tension (n = 9) at a rate of 0.5% /sec using a materials testing device. Apparent level yield stress, yield strain, Young's modulus (E), residual strain, inelastic strain and applied energy were determined from the stress-strain curve. After loading, specimens were stained with calcein (0.5 mM in PBS, 2 hours) to label microdamage caused by the applied load. The central 5 mm in length of each specimen was then cut away, and embedded undecalcified in methyl-methacrylate in preparation for serial milling imaging.

### Image acquisition, processing and analysis

Three-dimensional images of bone and fluorescent labels of microdamage were collected at a voxel size of 0.7 × 0.7 × 5.0 μm using serial milling (Slyfield et al., 2009; Slyfield et al., 2012; Tkachenko et al., 2009). As the image acquisition and pre-processing methodology has been well described previously (see Supplementary Materials for a summary), we concentrate here on image thresholding and analysis. To avoid damage caused during specimen preparation and, only the central region of each specimen was analyzed, resulting in a region of interest corresponding to 5.4 mm in diameter and 4 mm in height. Bone was segmented from each image using a manually determined global threshold. The bone surface was smoothed by closing with a spherical structuring element with a radius of 14 μm.

Images of microdamage were resampled to 2.8 × 2.8 × 2.5 μm to achieve more isotropic voxels (enabling morphological processing) and thresholds were determined manually. Regions stained with xylenol orange represented microdamage present before mechanical testing while the calcein stain identified pre-existing microdamage as well as microdamage caused by mechanical testing. Here we study only microdamage caused by applied loading (regions with calcein without xylenol orange). Measures of microdamage from serial milling do not differentiate among microdamage morphologies (microcracks, diffuse damage, etc.). Small amounts of non-specific staining (very thin stains on bone surfaces) that are ignored when making hand counts are also present. Microdamage stain within 5.6 μm of the bone surface was classified as non-specific staining and removed prior to automated analysis. A spherical structuring element with a radius of 2.8 μm was used to smooth the remaining fluorescent signal. Staining within a single microdamage site was not always contiguous due to small errors from thresholding. Patches of disconnected fluorescent microdamage signal were considered to be part of the same microdamage site if they were within 28 μm of each other. Microdamage sites smaller than 10,000 $\mu m^3$ (determined through analysis of image histograms ~ the volume of three osteocyte lacuna) were characterized as random noise and removed from the image. Removal of small damage sites altered damage volume by less than 10%. Damage volume fraction (DV/BV) was determined for each specimen.

Traditional bone microarchitecture measurements of the entire specimen were performed using IPL (V5.15, Scanco Medical Brüttisellen, Switzerland, see Table 1 for list of measures) after coarsening to a voxel size of 10 × 10 × 10 μm. The average trabecular thickness at regions of microdamage was determined using information from each bone voxel coincident with microdamage (trabecular thickness, Tb.Th at each voxel is an additional output from the IPL software). Percent eroded surface (ES/BS) was determined by point counting using three cross-sections of the raw gray-scale images (pixel size 0.7 × 0.7 μm) per specimen (grid size 200 μm). Image processing and visualization was performed using custom scripts written for use with Matlab (R2011b (Version 7.13), Mathworks, Natick, MA, USA) and Amira (5.3 Visage Imaging, San Diego, CA, USA).

### Spatial association of microdamage and eroded surfaces

In a previous study, the spatial correlation of microdamage and resorption cavities was determined using an “object based” method (Slyfield et al., 2012). Here we used a more refined “point based” spatial correlation assay. The method determined the likelihood that a

single voxel of microdamage is near a resorption cavity as well as the likelihood that a single voxel on a resorption cavity is near microdamage, using two distances: ½ the average trabecular thickness and the entire trabecular thickness (65 μm and 133 μm). Within each specimen, 30 voxels were selected at random from the microdamage volume and an identical number of voxels of bone tissue distant from microdamage were selected at random (Fig. 1A). The regions around each selected voxel (no regions overlapped) were displayed in three-dimensions to an observer blinded to the presence of microdamage. The observer then determined whether eroded surface was present within each region (Tkachenko et al., 2009). The proportion of voxels within microdamage with nearby eroded surface ($p_{damage}$) and the proportion of voxels distant from microdamage with nearby eroded surface ($p_{no\text{-}damage}$) were determined. A similar process was used to address the converse question: if a voxel on eroded surface was more likely to have microdamage nearby. As identification of all eroded surfaces would require excessive labor, only a sampling of eroded surface was examined; all eroded surfaces present within 9 cross-sections of the specimen (cross-sections were selected in a systemic random fashion) were identified, traced and viewed in three-dimensions to confirm the presence of eroded surface (8–37 independent eroded surfaces, 20 ± 6, mean ± SD). The proportion of voxels on eroded surface with microdamage nearby ($p_{eroded\ surface}$) and the proportion of bone surfaces without an eroded surface near microdamage ($p_{no\text{-}eroded\ surface}$) were determined (Fig. 1B).

### Statistical analysis

Differences in microdamage, mechanical properties and bone microarchitecture between tension and compression were determined using a paired t-test after confirmation of normality. A difference in volume of microdamage sites was determined using a mixed-design ANOVA, with tension or compression as between-subject variable and donor as a random factor (within-subjects variable). Correlation analysis was used to identify relationships between measures of microdamage, mechanical properties, and bone microarchitecture. The spatial correlations, expressed as relative risk ($p_{damage}/p_{no\text{-}damage}$ and $p_{eroded\ surface}/p_{no\text{-}eroded\ surface}$) were tested for differences from a value of 1.0 using a t-test, (a value of 1.0 indicates no spatial correlation). To confirm that the initial distribution of stress throughout trabecular microarchitecture did not bias the spatial correlation assay, finite element models were made from micro-computed tomography images of a subset of the specimens (n=15, see Supplementary Materials). Finite element models were used to determine the average maximum magnitude principal strain (*average* ($\max(|\varepsilon_1|,|\varepsilon_2|,|\varepsilon_3|)$) within each neighborhood examined during the spatial correlation analysis. A logarithmic regression model was generated to predict the probability of observing an eroded surface (when determining $p_{damage}$, $p_{no\text{-}damage}$) or the probability of detecting microdamage (when determining $p_{eroded\ surface}$, $p_{no\text{-}eroded\ surface}$) based on the interaction between local mechanical strain and the predictor variable. Statistical tests were conducted using JMP (v. 9, SAS Institute Inc., Cary, NC, USA).

## Results

The amount of microdamage (DV/BV) caused by loading to apparent yield was greater in specimens loaded in tension (3.9 ± 2.4%, mean ± SD) than compression (1.9 ± 1.3%, p =

0.01, Fig. 2A, Table 1). The volume of individual microdamage sites was greater ($p < 0.001$) in specimens loaded in tension as compared to compression (Fig. 2B), but the number of microdamage sites did not differ ($p = 0.64$) between specimens loaded in tension and compression (Fig. 2C).

Considerable between-donor variation in the overall amount of microdamage and size of individual microdamage sites was observed. Donors with greater DV/BV under compression showed increased DV/BV in tension ($p = 0.03$, Fig. 3A) and specimens with larger microdamage sites in compression also showed larger microdamage sites in tension ($p < 0.001$, Fig. 3B). Variation in DV/BV was dominated by between-donor differences; accounting for donor effects between specimens loaded in tension and compression resulted in increases in adjusted $R^2$ from 0.19 to 0.71. The effect of donor on Young's modulus and yield strength was negligible compared to the effect of BV/TV ($R^2$ reduced when including donor and negligible changes in regression coefficients). Donor age was not correlated with measures of microdamage.

Only subtle relationships between amounts of microdamage and whole specimen microarchitecture were observed. For specimens loaded in compression, DV/BV was negatively correlated with bone volume fraction ($r^2 = 0.52$, $p = 0.03$, Fig. 4B) and positively correlated with structure model index ($r^2 = 0.62$, $p = 0.01$, Table 2). In specimens loaded in tension, no correlations between BV/TV and DV/BV or size of individual microdamage sites were observed (Table 3). No differences in whole specimen microarchitecture were observed between specimens loaded in tension v. compression (Table 1). Whole specimen eroded surface (ES/BS) was negatively correlated with DV/BV generated in compression but was not correlated with DV/BV generated in tension (Fig 4A). Although there was no correlation between DV/BV and whole specimen average Tb.Th, local Tb.Th at voxels of microdamage were greater than at locations without microdamage (Fig. 4C, 4D).

Spatial correlation analysis did not detect an increased presence of resorption cavities near microdamage (Fig 5A) or increased presence of microdamage near resorption cavities (Fig 5B) (both ratios not significantly different from 1.0). The proportion of bone microdamage sites with resorption cavities did not differ between specimens loaded in tension and compression (Table S1). The average maximum magnitude strain in the neighborhood of each examined voxel did not influence conclusions regarding spatial correlations in tension ($p = 0.21$ for $p_{damage}$ and $p = 0.91$ for $p_{eroded\ surface}$) or in compression ($p = 0.67$ for $p_{eroded\ surface}$). An effect of average maximum magnitude strain was observed in specimens loaded in compression ($p = 0.04$) but suggested that average maximum magnitude strain only influenced the likelihood of detecting eroded surface at locations without microdamage ($p_{no\text{-}damage}$) with no effect at locations within microdamage ($p_{damage}$).

Measures of microdamage (DV/BV, size of microdamage sites, number of microdamage sites) were not correlated with apparent mechanical properties measured in the single load-unload cycle in tension (see list of mechanical properties in Table 1 and correlation matrix in Table S2). In compression, DV/BV correlated with residual strain in samples loaded in compression ($r^2 = 0.64$) but not to any other apparent mechanical properties (Table S3).

None of the measures of microdamage were correlated with post-yield strain or energy applied.

## Discussion

Microdamage generated during loading can greatly influence mechanical performance under subsequent loads (Hernandez et al., 2014). We found that loading mode influences microdamage amount and the size of microdamage sites and that traditional measures of microarchitecture have a relatively small influence on the amount of microdamage generated.

A strength of the current study was the use of a three-dimensional assay of microdamage, allowing the enumeration of individual microdamage sites as well as their size and location relative to local characteristics of microarchitecture including local Tb.Th and the presence of resorption cavities. Additionally, by using paired specimens from each donor it was possible to compare variation in microdamage among and between individuals. A limitation of the study is that microdamage is measured using fluorochrome bulk staining, which stains some but not all regions of permanent deflection in bone tissue (Sun et al., 2010).

The differences in amounts of microdamage between apparent tension and compression observed here are consistent with results from high-resolution finite element analyses that showed more tissue failure for apparent tension or shear than apparent compression loading (Bayraktar and Keaveny, 2004; Sanyal et al., 2012), thereby providing support for the tissue-level asymmetric tensile-compressive principal strain failure criteria approach used in the models. Mechanical loading of individual trabeculae also supports the asymmetric failure criteria (Jungmann et al., 2011). Our finding that apparent tension results in larger microdamage sites rather than an increase in number of microdamage sites suggests that microdamage sites were more likely to extend under apparent tension. Under apparent tension or shear, tissue failure occurs entirely from excessive tensile principal strains, while under apparent compression, tissue failure occurs through both tensile and compressive tissue yielding, with a greater tensile tissue yielding component in bone with a lower bone volume fraction (Bayraktar and Keaveny, 2004; Sanyal et al., 2012). The increased microdamage site size under apparent tension supports the idea that microdamage initiation and propagation in cancellous bone tissue may be closely related to mode-I fracture toughness (tensile opening). Which might suggest failure mode differences from cortical bone tissue, in which microdamage has been shown to be more sensitive to mode II/mixed loading (Zimmermann et al., 2010). A detailed stress analysis would be required to confirm differences in failure modes between trabecular and cortical bone tissue.

The current study demonstrates a strong effect of donor characteristics other than bone microarchitecture on the generation of microdamage in both loading modes. Variance in apparent mechanical properties of cancellous bone such as Young's modulus and strength is explained primarily by bone volume fraction or related measures of microarchitecture (Keaveny et al., 2001). Consistent with prior work, donor had very little effect on the relationship between apparent Young's modulus and bone volume fraction in the current study. However, the effect of donor on microdamage generation in the current study was

independent of bone volume fraction, traditional microarchitecture measures, apparent Young's modulus and apparent yield strength (Table S4, S5). Our findings therefore illustrate how two otherwise healthy donors may have cancellous bone with similar apparent strength, but large differences in the amount of microdamage generated during the same type of monotonic overload. Cancellous bone with more microdamage demonstrates greater reductions in strength, stiffness and fatigue life under subsequent loading (Hernandez et al., 2014; Lambers et al., 2013; Wachtel and Keaveny, 1997b). Hence, cancellous bone from an individual with high propensity to microdamage may not display reductions in stiffness/strength under a single load (the most common biomechanical test). Identifying those individuals (and the associated alterations in tissue material properties) instead requires testing with multiple loads and/or microdamage analysis — a technically challenging task. Some aspects of tissue-level material properties can be probed using nano/microindentation methods (Donnelly, 2011; Lewis and Nyman, 2008), although it remains unclear how indentation measurements are related to microcrack/microdamage initiation and propagation and/or fracture toughness (Lewis and Nyman, 2008; Thurner, 2009).

Cancellous bone loaded in compression did show increased microdamage in specimens with lower BV/TV (and a more rod-like structure as assessed with SMI). Several prior studies have shown correlations between microdamage and bone microstructure (Arlot et al., 2008; Follet et al., 2013; Karim and Vashishth, 2011, 2012; Wang and Niebur, 2006). We attribute the relationship between BV/TV and microdamage to regions of local tensile strain. Cancellous bone loaded in apparent compression experiences regions of compression and tension due to bending of individual trabeculae. Specimens of cancellous bone with lower BV/TV undergo greater bending deflections (Bevill et al., 2006) resulting in more regions of local tensile strain (Sanyal et al., 2012) and therefore more microdamage (greater DV/BV). When cancellous bone is loaded in tension, however, tissue level strains are almost exclusively tensile irrespective of BV/TV (Bayraktar and Keaveny, 2004), explaining why no trend between DV/BV and BV/TV was observed.

We found that local trabecular thickness at sites of microdamage was greater than the average trabecular thickness overall. The finding suggests that microdamage is not necessarily occurring in the thinnest trabeculae – as one might expect if damage were to follow a weakest-link paradigm – and may instead be occurring at thicker trabeculae and/or nodes within the trabecular microstructure. At nodes, stresses are multidirectional, through which microdamage potentially extends more easily through microstructural barriers than at locations where stresses are unidirectional (Wang et al., 2005). The finding that microdamage occurs at thicker trabeculae is consistent with finite element models suggesting that tissue yielding occurred predominantly in plate-like trabeculae, and less in rod-like trabeculae (Shi et al., 2010) and contradicts a prior study that found regions of microdamage to be associated with thinner trabeculae (Green et al., 2011). A likely explanation for differences between our finding and others is that the current study used three-dimensional assessment of microdamage volume and trabecular thickness through the whole region of interest while others have used two-dimensional assessments of microdamage (classifying microdamage qualitatively).

The current study did not observe any significant spatial association between microdamage and resorption cavities. In a previous paper from our group, we reported an association between microdamage and resorption cavities (Slyfield et al., 2012). We consider the current study to be a better assessment of spatial correlations between microdamage and resorption cavities in that the current study has a larger sample size and used a more refined method of assessing spatial correlations. The local strain distribution (determined with high-resolution finite element models) did not alter our conclusions regarding spatial correlations with resorption cavities. Furthermore, DV/BV was greater in specimens having lower amounts of eroded surface, suggesting that resorption cavities may have limited ability to promote microdamage in cancellous bone. The current study did not evaluate characteristics of resorption cavity size, and cavity size relative to local trabecular thickness. It remains possible that cavities that are large relative to local trabecular thickness promote microdamage generation.

## Supplementary Material

Refer to Web version on PubMed Central for supplementary material.

## Acknowledgments

This publication was made possible by Grant Number R01 AR057362 from NIAMS/NIH (PI CJH). We acknowledge use of human vertebral bodies provided by the National Disease Research Interchange (NDRI), with support from NIH grant 8U42OD011158-22. We thank Ivana H. Yi and Michael G. Jekir for performing the mechanical tests.

## References

Arlot ME, Burt-Pichat B, Roux JP, Vashishth D, Bouxsein ML, Delmas PD. Microarchitecture influences microdamage accumulation in human vertebral trabecular bone. J. Bone Miner. Res. 2008; 23:1613–1618. [PubMed: 18518771]

Bayraktar HH, Keaveny TM. Mechanisms of uniformity of yield strains for trabecular bone. J. Biomech. 2004; 37:1671–1678. [PubMed: 15388309]

Bevill G, Eswaran SK, Farahmand F, Keaveny TM. The influence of boundary conditions and loading mode on high-resolution finite element-computed trabecular tissue properties. Bone. 2009; 44:573–578. [PubMed: 19110082]

Bevill G, Eswaran SK, Gupta A, Papadopoulos P, Keaveny TM. Influence of bone volume fraction and architecture on computed large-deformation failure mechanisms in human trabecular bone. Bone. 2006; 39:1218–1225. [PubMed: 16904959]

Bigley RF, Singh M, Hernandez CJ, Kazakia GJ, Martin RB, Keaveny TM. Validity of serial milling-based imaging system for microdamage quantification. Bone. 2008; 42:212–215. [PubMed: 17951125]

Burr DB, Forwood MR, Fyhrie DP, Martin RB, Schaffler MB, Turner CH. Bone microdamage and skeletal fragility in osteoporotic and stress fractures. J Bone Miner Res. 1997; 12:6–15. [PubMed: 9240720]

Donnelly E. Methods for assessing bone quality: a review. Clin Orthop Relat Res. 2011; 469:2128–2138. [PubMed: 21116752]

Follet H, Farlay D, Bala Y, Viguet-Carrin S, Gineyts E, Burt-Pichat B, Wegrzyn J, Delmas P, Boivin G, Chapurlat R. Determinants of microdamage in elderly human vertebral trabecular bone. PLoS One. 2013; 8:e55232. [PubMed: 23457465]

Green JO, Nagaraja S, Diab T, Vidakovic B, Guldberg RE. Age-related changes in human trabecular bone: Relationship between microstructural stress and strain and damage morphology. J. Biomech. 2011; 44:2279–2285. [PubMed: 21724189]

Herman BC, Cardoso L, Majeska RJ, Jepsen KJ, Schaffler MB. Activation of bone remodeling after fatigue: differential response to linear microcracks and diffuse damage. Bone. 2010; 47:766–772. [PubMed: 20633708]

Hernandez CJ, Keaveny TM. A biomechanical perspective on bone quality. Bone. 2006; 39:1173–1181. [PubMed: 16876493]

Hernandez CJ, Lambers FM, Widjaja J, Chapa C, Rimnac CM. Quantitative relationships between microdamage and cancellous bone strength and stiffness. Bone. 2014; 66:205–213. [PubMed: 24928495]

Jungmann R, Szabo ME, Schitter G, Yue-Sing Tang R, Vashishth D, Hansma PK, Thurner PJ. Local strain and damage mapping in single trabeculae during three-point bending tests. J Mech Behav Biomed Mater. 2011; 4:523–534. [PubMed: 21396601]

Karim L, Vashishth D. Role of trabecular microarchitecture in the formation, accumulation, and morphology of microdamage in human cancellous bone. J Orthop Res. 2011; 29:1739–1744. [PubMed: 21538510]

Karim L, Vashishth D. Heterogeneous glycation of cancellous bone and its association with bone quality and fragility. PLoS One. 2012; 7:e35047. [PubMed: 22514706]

Keaveny TM, Morgan EF, Niebur GL, Yeh OC. Biomechanics of trabecular bone. Annu Rev Biomed Eng. 2001; 3:307–333. [PubMed: 11447066]

Lambers FM, Bouman AR, Rimnac CM, Hernandez CJ. Microdamage caused by fatigue loading in human cancellous bone: relationship to reductions in bone biomechanical performance. PLoS One. 2013; 8:e83662. [PubMed: 24386247]

Lewis G, Nyman JS. The use of nanoindentation for characterizing the properties of mineralized hard tissues: state-of-the art review. J Biomed Mater Res B Appl Biomater. 2008; 87:286–301. [PubMed: 18395829]

Moore TL, Gibson LJ. Fatigue microdamage in bovine trabecular bone. J Biomech Eng. 2003; 125:769–776. [PubMed: 14986400]

Moore TLA, Gibson LJ. Microdamage accumulation in bovine trabecular bone in uniaxial compression. J Biomech Eng-T Asme. 2002; 124:63–71.

Mori S, Burr DB. Increased intracortical remodeling following fatigue damage. Bone. 1993; 14:103–109. [PubMed: 8334026]

Sanyal A, Gupta A, Bayraktar HH, Kwon RY, Keaveny TM. Shear strength behavior of human trabecular bone. Journal of biomechanics. 2012; 45:2513–2519. [PubMed: 22884967]

Shi X, Liu XS, Wang X, Guo XE, Niebur GL. Effects of trabecular type and orientation on microdamage susceptibility in trabecular bone. Bone. 2010; 46:1260–1266. [PubMed: 20149908]

Silva MJ, Gibson LJ. Modeling the mechanical behavior of vertebral trabecular bone: Effects of age-related changes in microstructure. Bone. 1997; 21:191–199. [PubMed: 9267695]

Slyfield CR Jr. Niemeyer KE, Tkachenko EV, Tomlinson RE, Steyer GG, Patthanacharoenphon CG, Kazakia GJ, Wilson DL, Hernandez CJ. Three-dimensional surface texture visualization of bone tissue through epifluorescence-based serial block face imaging. J Microsc. 2009; 236:52–59. [PubMed: 19772536]

Slyfield CR, Tkachenko EV, Fischer SE, Ehlert KM, Yi IH, Jekir MG, O'Brien RG, Keaveny TM, Hernandez CJ. Mechanical failure begins preferentially near resorption cavities in human vertebral cancellous bone under compression. Bone. 2012; 50:1281–1287. [PubMed: 22426306]

Sun X, Hoon Jeon J, Blendell J, Akkus O. Visualization of a phantom post-yield deformation process in cortical bone. J Biomech. 2010; 43:1989–1996. [PubMed: 20382387]

Tang SY, Vashishth D. A non-invasive in vitro technique for the three-dimensional quantification of microdamage in trabecular bone. Bone. 2007; 40:1259–1264. [PubMed: 17329178]

Tang SY, Vashishth D. Non-enzymatic glycation alters microdamage formation in human cancellous bone. Bone. 2010; 46:148–154. [PubMed: 19747573]

Thurner PJ. Atomic force microscopy and indentation force measurement of bone. Wiley Interdiscip Rev Nanomed Nanobiotechnol. 2009; 1:624–649. [PubMed: 20049821]

Tkachenko EV, Slyfield CR, Tomlinson RE, Daggett JR, Wilson DL, Hernandez CJ. Voxel size and measures of individual resorption cavities in three-dimensional images of cancellous bone. Bone. 2009; 45:487–492. [PubMed: 19482097]

Vashishth D, Koontz J, Qiu SJ, Lundin-Cannon D, Yeni YN, Schaffler MB, Fyhrie DP. In vivo diffuse damage in human vertebral trabecular bone. Bone. 2000; 26:147–152. [PubMed: 10678409]

Wachtel EF, Keaveny TM. Dependence of trabecular damage on mechanical strain. J. Orthop. Res. 1997a; 15:781–787. [PubMed: 9420610]

Wachtel EF, Keaveny TM. Dependence of trabecular damage on mechanical strain. J Orthop Res. 1997b; 15:781–787. [PubMed: 9420610]

Wang X, Guyette J, Liu X, Roeder RK, Niebur GL. Axial-shear interaction effects on microdamage in bovine tibial trabecular bone. European journal of morphology. 2005; 42:61–70. [PubMed: 16123025]

Wang X, Niebur GL. Microdamage propagation in trabecular bone due to changes in loading mode. J Biomech. 2006; 39:781–790. [PubMed: 16488217]

Wu Z, Laneve AJ, Niebur GL. In vivo microdamage is an indicator of susceptibility to initiation and propagation of microdamage in human femoral trabecular bone. Bone. 2013; 55:208–215. [PubMed: 23459314]

Yeh OC, Keaveny TM. The relative roles of microdamage and microfracture in the mechanical behavior of trabecular bone. J. Orthop. Res. 2001; 19:1001–1007. [PubMed: 11780997]

Zimmermann EA, Launey ME, Ritchie RO. The significance of crack-resistance curves to the mixed-mode fracture toughness of human cortical bone. Biomaterials. 2010; 31:5297–5305. [PubMed: 20409579]

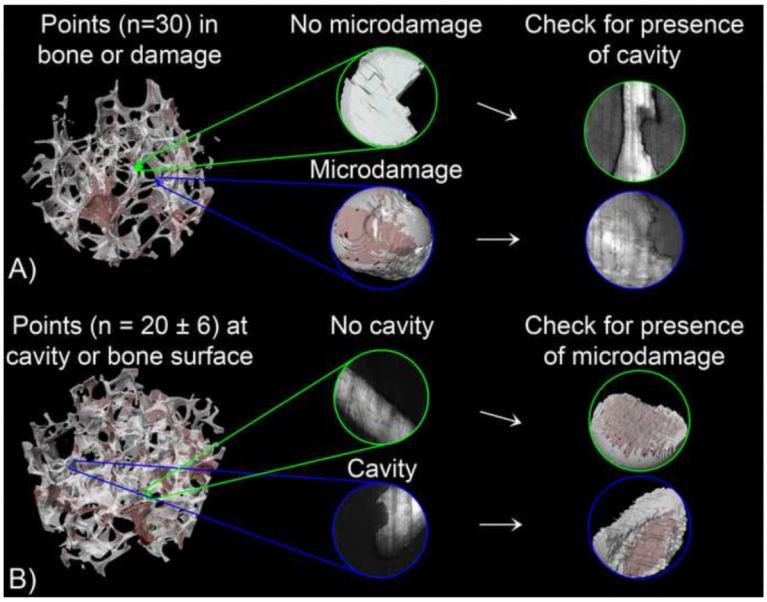


**Figure 1.**

A) The spatial correlation between microdamage and eroded surfaces was determined by selecting at random 30 points at locations of damage and 30 points distant from microdamage and determining if an eroded surface was nearby. B) The spatial correlation between eroded surfaces and microdamage was determined by selecting points on the bone surface within an eroded surface or distant from an eroded surface and determining if microdamage was nearby.

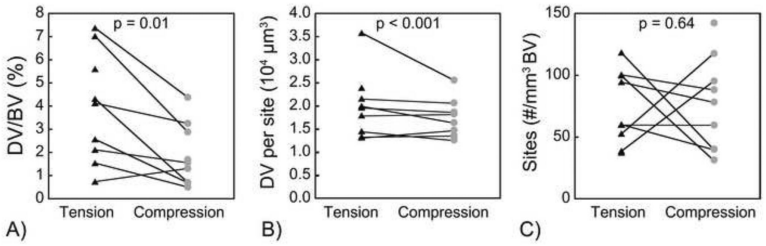


**Figure 2.**

Differences in A) whole specimen DV/BV; B) volume of each damage site; and C) number of damage sites between specimens loaded in tension and compression. Lines connect specimens from the same donor. p value indicates significant difference between tension and compression (paired t-test).

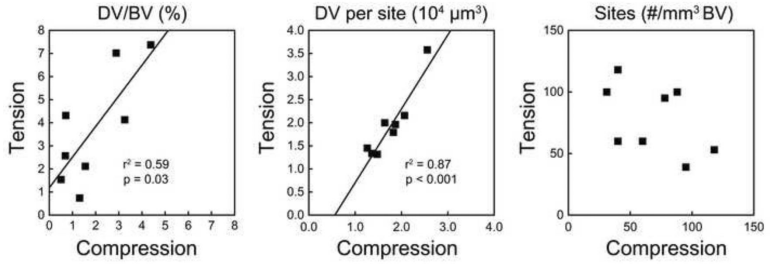


**Figure 3.**

DV/BV sustained in tension was positively correlated with DV/BV generated in compression from the same donor ($DV/BV_{tension} = 1.2 + 1.3 * DV/BV_{compression}$). The median damage volume of microdamage sites generated from tension was related to that generated in compression ($DV\ site_{tension} = 1.6 * DV\ site_{compression} - 9 \times 10^3$). The number of damage sites per bone volume was not related between tension and compression.

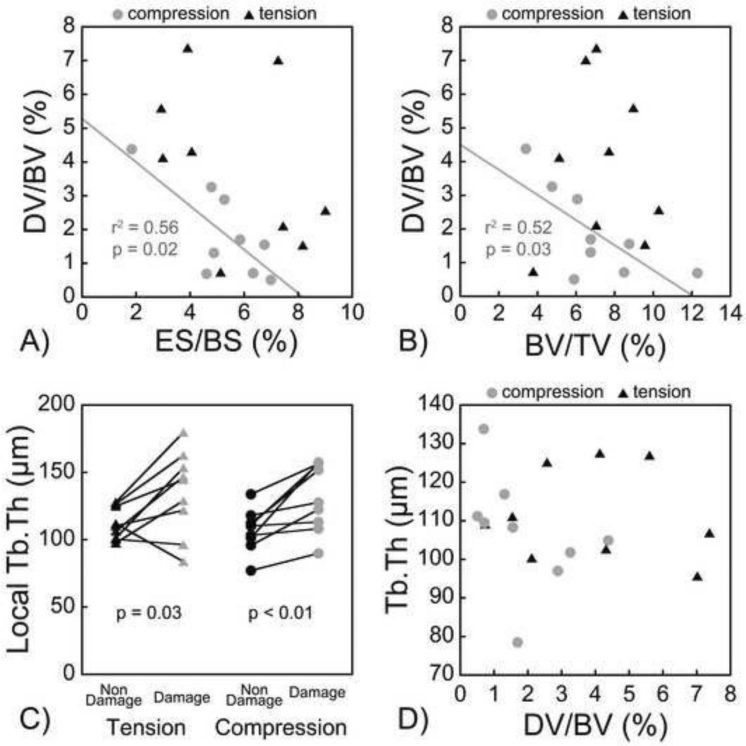


**Figure 4.**

A) DV/BV was negatively correlated with ES/BS in specimens subjected to compression (DV/BV = 5.3 − 0.6 * ES/BS), and not correlated with specimens subjected to tension. B) DV/BV was negatively correlated with BV/TV in specimens subjected to compression (DV/BV = 4.5 − 0.4 * BV/TV), and not correlated in specimens subjected to tension. C) Regions of microdamage had larger local Tb.Th although D) overall DV/BV was not correlated with average Tb.Th.

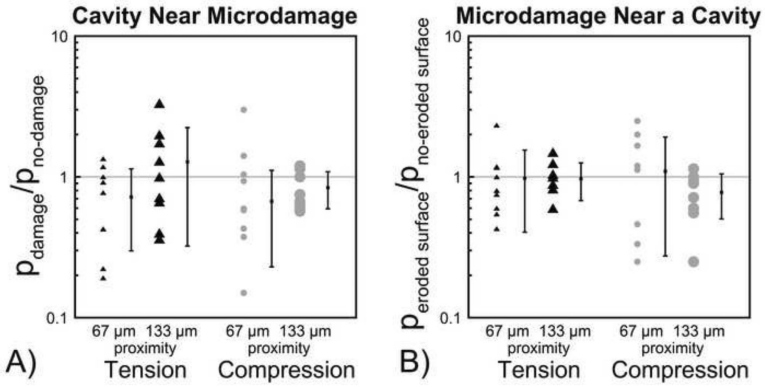


**Figure 5.**

A) The relative risk of finding an eroded surface around microdamage ($p_{damage}/p_{no\text{-}damage}$) and B) The relative risk of finding microdamage around an eroded surface are shown ($p_{eroded\ surface}/p_{no\text{-}eroded\ surface}$). The mean value for each relative risk is shown with error bars indicating the standard deviation. No significant differences from 1 were observed indicating no observable spatial correlations between microdamage and eroded surfaces.

## Table 1

Measures of microdamage, microarchitecture, and apparent mechanical properties are shown. Results are shown as mean (95% confidence interval). p value indicates significant difference between tension and compression. Tests assessing damage volume per microdamage site include all microdamage sites (not a specimen average).

| | Tension (n=9) | Compression (n=9) | p-value |
|---|---|---|---|
| **Microdamage** | | | |
| Damage Volume Fraction (DV/BV, %) | 3.93 (2.10, 5.77) | 1.89 (0.86, 2.92) | 0.01 |
| Number of damage sites (#) | 511 (294, 727) | 478 (261, 695) | 0.72 |
| Number of damage sites per bone volume (#/mm$^3$) | 74 (51, 97) | 77 (48, 106) | 0.64 |
| Damage volume per microdamage site($10^5$ μm$^3$) | 5.2 (4.0, 6.4) | 2.1 (1.6, 2.6) | < 0.001 |
| **Microarchitecture** | | | |
| Bone volume fraction (BV/TV,%) | 7.34 (5.73, 8.94) | 7.02 (5.03, 9.00) | 0.80 |
| Bone volume (BV, mm$^3$) | 6.72 (5.25, 8.19) | 6.42 (4.60, 8.24) | 0.80 |
| Bone surface (BS, mm$^2$) | 168 (141, 196) | 160 (124, 196) | 0.58 |
| Trabecular thickness (Tb.Th, μm) | 112 (102, 121) | 107 (95, 118) | 0.73 |
| Trabecular separation (Tb.Sp, mm) | 1.00 (0.90, 1.10) | 1.06 (0.90, 1.22) | 0.42 |
| Trabecular number (Tb.N, 1/mm) | 1.06 (0.96, 1.16) | 1.01 (0.86, 1.17) | 0.46 |
| Structure model index (SMI) | 1.60 (1.21, 1.99) | 1.46 (1.10, 1.82) | 0.41 |
| Degree of anisotropy (DA) | 1.40 (1.28, 1.53) | 1.54 (1.32, 1.75) | 0.24 |
| Connectivity density (Conn.D, 1/mm$^3$) | 3.75 (2.83, 4.66) | 3.22 (1.93, 4.52) | 0.37 |
| **Apparent Mechanical properties** | | | |
| Young's modulus (N/mm$^2$) | 276 (217, 336) | 231 (202, 260) | 0.15 |
| Yield strain (%) | 0.73 (0.70, 0.76) | 0.75 (0.71, 0.78) | 0.41 |
| Yield stress (N/mm$^2$) | 1.48 (1.20, 1.76) | 1.19 (0.99, 1.39) | 0.07 |
| Applied strain (%) | 0.81 (0.76, 0.86) | 0.84 (0.77, 0.91) | 0.43 |
| Residual strain (%) | 0.095 (0.085, 0.105) | 0.140 (0.165, 0.115) | <0.01 |
| Inelastic strain (%) | 0.25 (0.22, 0.28) | 0.25 (0.23, 0.28) | 0.90 |
| Energy Applied (mJ/mm$^3$) | 0.0072 (0.0058, 0.0085) | 0.0066 (0.0053, 0.0079) | 0.52 |

**Table 2**

Correlations between microarchitecture and microdamage generated under compression are shown. The upper triangle shows the value of r while the lower triangle displays the 95% confidence interval of r.

| | DV/BV (%) | Number of microdamage sites (#) | Number of microdamage sites per bone volume (#/mm$^3$) | Mean damage volume per microdamage site (μm$^3$) | Median damage volume per microdamage site (μm$^3$) | Bone volume fraction (%) | Bone surface (mm$^2$) | Trabecular thickness (μm) | Trabecular separation (mm) | Trabecular number (1/mm) | Structure model index (-) |
|---|---|---|---|---|---|---|---|---|---|---|---|
| **DV/BV (%)** | 1.00 | −0.23 | 0.41 | **−0.75*** | 0.30 | **−0.72*** | −0.60 | −0.40 | 0.12 | −0.25 | **0.79*** |
| **Number of microdamage sites (#)** | (−0.78, 0.51) | 1.00 | **0.67*** | −0.59 | −0.39 | 0.56 | **0.72*** | 0.12 | **−0.67*** | **0.76*** | −0.04 |
| **Number of microdamage sites per bone volume (#/mm$^3$)** | (−0.34, 0.85) | (0.02, 0.92) | 1.00 | −0.21 | −0.27 | −0.21 | 0.04 | −0.36 | −0.27 | 0.23 | 0.36 |
| **Mean damage volume per microdamage site (μm$^3$)** | (0.17, 0.94) | (−0.90, 0.11) | (−0.77, 0.53) | 1.00 | 0.61 | −0.52 | −0.48 | −0.32 | 0.11 | −0.27 | 0.48 |
| **Median damage volume per microdamage site (μm$^3$)** | (−0.46, 0.80) | (−0.84, 0.37) | (−0.79, 0.48) | (−0.09, 0.91) | 1.00 | −0.16 | −0.14 | −0.10 | −0.13 | 0.05 | 0.22 |
| **Bone volume fraction (%)** | (−0.94, −0.11) | (−0.17, 0.89) | (−0.77, 0.53) | (−0.88, 0.22) | (−0.74, 0.57) | 1.00 | **0.92*** | 0.57 | −0.64 | **0.76*** | −0.43 |
| **Bone surface (mm$^2$)** | (−0.90, 0.10) | (0.11, 0.94) | (−0.64, 0.69) | (−0.87, 0.27) | (−0.74, 0.58) | (0.66, 0.98) | 1.00 | 0.26 | **−0.83*** | **0.89*** | −0.42 |
| **Trabecular thickness (μm)** | (−0.84, 0.36) | (−0.59, 0.73) | (−0.83, 0.40) | (−0.81, 0.44) | (−0.71, 0.61) | (−0.15, 0.9) | (−0.49, 0.79) | 1.00 | −0.05 | 0.26 | 0.14 |
| **Trabecular separation (mm)** | (−0.59, 0.73) | (−0.92, −0.01) | (−0.79, 0.48) | (−0.6, 0.72) | (−0.73, 0.58) | (−0.91, 0.05) | (−0.96, −0.36) | (−0.69, 0.63) | 1.00 | **−0.95*** | −0.04 |
| **Trabecular number (1/mm)** | (−0.79, 0.49) | (0.18, 0.95) | (−0.51, 0.78) | (−0.79, 0.48) | (−0.64, 0.69) | (0.20, 0.95) | (0.55, 0.98) | (−0.49, 0.79) | (−0.99, −0.78) | 1.00 | 0.02 |
| **Structure model index (-)** | (0.27, 0.95) | (−0.68, 0.64) | (−0.40, 0.83) | (−0.27, 0.87) | (−0.52, 0.77) | (−0.85, 0.33) | (−0.85, 0.34) | (−0.58, 0.74) | (−0.68, 0.64) | (−0.65, 0.68) | 1.00 |

**Table 3**

Correlations between microarchitecture and microdamage generated under tension are shown. The upper triangle shows the value of r while the lower triangle displays the 95% confidence interval of r.

| | DV/BV (%) | Number of microdamage sites (#) | Number of Microdamage sites per bone volume (#/mm$^3$) | Mean damage volume per microdamage site (μm$^3$) | Median damage volume per microdamage site (μm$^3$) | Bone volume fraction (%) | Bone surface (mm$^2$) | Trabecular thickness (μm) | Trabecular separation (mm) | Trabecular number (1/mm) | Structure model index (-) |
|---|---|---|---|---|---|---|---|---|---|---|---|
| **DV/BV (%)** | 1.00 | −0.40 | −0.43 | **0.92*** | 0.61 | 0.04 | 0.28 | −0.13 | **−0.69*** | 0.60 | 0.18 |
| **Number of microdamage sites (#)** | (−0.84, 0.36) | 1.00 | **0.87*** | −0.54 | −0.44 | **0.71*** | 0.64 | 0.13 | −0.30 | 0.35 | **−0.75*** |
| **Number of microdamage sites per bone volume (#/mm$^3$)** | (−0.85, 0.33) | (0.48, 0.97) | 1.00 | −0.54 | −0.40 | 0.31 | 0.30 | 0.05 | −0.07 | 0.11 | −0.49 |
| **Mean damage volume per microdamage site (μm$^3$)** | (0.64, 0.98) | (−0.89, 0.19) | (−0.92, 0.00) | 1.00 | 0.60 | 0.08 | 0.20 | −0.03 | −0.53 | 0.42 | 0.16 |
| **Median damage volume per microdamage site (μm$^3$)** | (−0.08, 0.91) | (−0.86, 0.31) | (−0.84, 0.35) | (−0.10, 0.90) | 1.00 | −0.19 | 0.12 | −0.56 | −0.18 | 0.11 | 0.16 |
| **Bone volume fraction (%)** | (−0.64, 0.68) | (0.08, 0.93) | (−0.45, 0.81) | (−0.62, 0.71) | (−0.76, 0.54) | 1.00 | **0.89*** | 0.26 | −0.60 | 0.58 | **−0.83*** |
| **Bone surface (mm$^2$)** | (−0.47, 0.80) | (−0.04, 0.92) | (−0.46, 0.80) | (−0.54, 0.76) | (−0.59, 0.73) | (0.54, 0.98) | 1.00 | −0.09 | **−0.79*** | **0.79*** | **−0.75*** |
| **Trabecular thickness (μm)** | (−0.73, 0.59) | (−0.58, 0.73) | (−0.64, 0.69) | (−0.68, 0.65) | (−0.89, 0.17) | (−0.49, 0.79) | (−0.71, 0.61) | 1.00 | −0.06 | 0.03 | 0.11 |
| **Trabecular separation (mm)** | (−0.93, −0.04) | (−0.8, 0.46) | (−0.70, 0.62) | (−0.88, 0.21) | (−0.75, .55) | (−0.90, 0.11) | (−0.95, −0.27) | (−0.69, 0.63) | 1.00 | **−0.98*** | 0.28 |
| **Trabecular number (1/mm)** | (−0.11, 0.90) | (−0.41, 0.82) | (−0.60, 0.72) | (−0.34, 0.85) | (−0.60, 0.72) | (−0.14, 0.90) | (0.26, 0.95) | (−0.65, 0.68) | (−1.00, −0.91) | 1.00 | −0.26 |
| **Structure model index (-)** | (−0.55, 0.75) | (−0.94, −0.17) | (−0.87, 0.25) | (−0.56, 0.75) | (−0.57, 0.74) | (−0.96, −0.38) | (−0.94, −0.17) | (−0.60, 0.72) | (−0.47, 0.80) | (−0.79, 0.49) | 1.00 |